Nature of the absorbing gas associated with a galaxy group at $z \sim 0.4$

Céline Péroux,[1][*] Hadi Rahmani,[1] Samuel Quiret,[1] Max Pettini,[2] Varsha Kulkarni,[3] Donald G. York,[4] Lorrie Straka,[5] Bernd Husemann[6] and Bruno Milliard[1]

[1]*Aix Marseille Université, CNRS, LAM (Laboratoire d'Astrophysique de Marseille) UMR 7326, F-13388 Marseille, France*
[2]*Institute of Astronomy, University of Cambridge, Madingley Road, Cambridge CB3 0HA, UK*
[3]*Department of Physics and Astronomy, University of South Carolina, Columbia, SC 29208, USA*
[4]*Department of Astronomy and Astrophysics and The Enrico Fermi Institute, University of Chicago, 5640 S. Ellis Ave, Chicago, IL 60637, USA*
[5]*Sterrewacht Leiden, Leiden University, PO Box 9513, NL-2300 RA Leiden, the Netherlands*
[6]*European Southern Observatory (ESO), Karl-Schwarzschild-Str. 2, D-85748 Garching bei München, Germany*

ABSTRACT

We present new Multi Unit Spectroscopic Explorer observations of quasar field Q2131−1207 with a log N(H I) $= 19.50 \pm 0.15$ sub-damped Lyman α at $z_{\rm abs} = 0.42980$. We detect four galaxies at a redshift consistent with that of the absorber where only one was known before this study. Two of these are star-forming galaxies, while the ones further away from the quasar (>140 kpc) are passive galaxies. We report the metallicities of the H II regions of the closest objects ($12 + \log$(O/H) $= 8.98 \pm 0.02$ and 8.32 ± 0.16) to be higher or equivalent within the errors to the metallicity measured in absorption in the neutral phase of the gas (8.15 ± 0.20). For the closest object, a detailed morphokinematic analysis indicates that it is an inclined large rotating disc with $V_{\rm max} = 200 \pm 3$ km s^{-1}. We measure the masses to be $M_{\rm dyn} = 7.4 \pm 0.4 \times 10^{10}$ M$_\odot$ and $M_{\rm halo} = 2.9 \pm 0.2 \times 10^{12}$ M$_\odot$. Some of the gas seen in absorption is likely to be corotating with the halo of that object, possibly due to a warped disc. The azimuthal angle between the quasar line-of-sight and the projected major axis of the galaxy on the sky is $12° \pm 1°$ which indicates that some other fraction of the absorbing gas might be associated with accreting gas. This is further supported by the galaxy to gas metallicity difference. Based on the same arguments, we exclude outflows as a possibility to explain the gas in absorption. The four galaxies form a large structure (at least 200 kpc wide) consistent with a filament or a galaxy group so that a fraction of the absorption could be related to intragroup gas.

Key words: galaxies: abundances – intergalactic medium – galaxies: ISM – galaxies: kinematics and dynamics – quasars: absorption lines.

1 INTRODUCTION

One of the key unknowns in the study of galaxy evolution is how galaxies acquire their gas and how they exchange this gas with their surroundings. Since gas, stars and metals are intimately connected, gas flows affect the history of star formation and chemical enrichment in galaxies. Accretion is required to explain some of the basic observed properties of galaxies including the gas-phase metallicity (Erb et al. 2006). Moreover, galaxies are believed to interact with the intergalactic medium (IGM) by pervading it with hydrogen ionizing photons and by injecting heavy elements formed in stars and supernovae through supersonic galactic winds. Indeed, observations of the IGM indicate significant quantities of metals at all redshifts (Pettini 2003; Ryan-Weber et al. 2009; D'Odorico

et al. 2013; Shull, Danforth & Tilton 2014; Becker, Bolton & Lidz 2015). The presence of these metals is interpreted as a signature of strong galactic outflows in various models (Aguirre et al. 2001; Oppenheimer & Davé 2006). Hydrodynamical simulations provide predictions of the physical properties of these gas flows (Keres et al. 2005; Brook et al. 2011; Keating et al. 2015). In recent years, much attention has been focused on the circumgalactic medium (CGM), a loosely defined term that describes the gas immediately surrounding galaxies over scales of $\sim$300 kpc (Shull 2014). The CGM is at the heart of these physical processes. Therefore, study of the CGM is crucial for understanding both the inflows of gas accreting into galaxies and the outflows carrying away the energy and metals generated inside galaxies.

Outflows are commonly probed by the presence of interstellar absorption lines from cool gas blueshifted by hundreds of km s^{-1} relative to the systemic velocities of the background galaxies (Shapley et al. 2003; Steidel et al. 2010). Strong Mg II absorbers in particular

(Martin et al. 2012; Schroetter et al. 2015) have been observed to extend out to 100 kpc along the galaxies' minor axes (Bordoloi et al. 2011), a fraction of which could be associated with galactic winds. Outflows are ubiquitous in galaxies at various redshifts (Pettini et al. 2001, 2002; Cabanac, Valls-Gabaud & Lidman 2008; Heckman et al. 2015). Interestingly, the circumgalactic gas has also been probed in emission by Steidel et al. (2011) who stacked narrow-band images of $z \sim 2$–3 galaxies and revealed diffuse Lyα haloes extending to 80 kpc. More recently, the Guaranteed Time Observations (GTO) Multi Unit Spectroscopic Explorer (MUSE) team used a 27-h deep field to report Lyα haloes in individual emitters down to a limiting surface brightness of $\sim 10^{-19}$ erg s^{-1} cm^{-2} arcsec^{-2} with a scale length of a few kpc (Wisotzki et al. 2016).

While observational evidence for outflows is growing, direct probes of infall are notoriously more difficult to gather. So far, the accretion of cool gaseous material has been directly observed only in the Milky Way in high-velocity clouds in 21 cm emission at distances of 5–20 kpc (Lehner & Howk 2011; Richter et al. 2014). At larger distances, nearby spirals exhibit both extraplanar H I clouds and morphological disturbances, which may be attributed to gas infall (Sancisi et al. 2008). However, the emission from these diffuse structures is difficult to map at high redshift. Nevertheless, detections suggestive of cool gas inflows have recently been reported in a few objects (Rubin et al. 2011; Martin et al. 2012; Bouché et al. 2013; Diamond-Stanic et al. 2016).

A powerful tool to study the CGM gas is offered by absorption lines in quasar spectra. We have initiated a novel technique to examine this gas in absorption against background sources whose lines of sight pass through the CGM of galaxies using 3D spectroscopy (Bouché et al. 2007; Péroux et al. 2011a). Over the past few years, we have demonstrated the power of this technique for studying the CGM using Very Large Telescope (VLT)/Spectrograph for Integral Field Observations in the Near Infrared (SINFONI) by successfully detecting the galaxies responsible for strong N(H I) absorbers at redshifts $z \sim 1$ and ~ 2 (Péroux et al. 2011b, 2012, 2013, 2016; Péroux, Kulkarni & York 2014). These detections have enabled us to map the kinematics, star formation rate (SFR) and metallicity of this emitting gas, and to estimate the dynamical masses of these galaxies. Out of our six detections for absorbers with known N(H I), we find evidence for the presence of outflows in two of them, while three are consistent with gas accretion. The remaining system at $z \sim 2$ is poorly constrained (Péroux et al. 2016).

Having demonstrated the power of 3D spectroscopy for study of the CGM at high-z (Péroux et al. 2016), we now extend the technique at low redshift with the MUSE optical spectrograph. Here, we present results from new observations of a sub-damped Lyman α (DLA) at $z_{abs} = 0.42980$. The paper is organized as follows. Section 2 presents the ancillary and new observations of the absorber and the quasar field. Section 3 shows the analysis performed on the new MUSE and ancillary observations presented here. Finally, in Section 4, we explore different scenarios to explain the gas seen in absorption in relation with the objects observed in the field. Throughout this paper we adopt an $H_0 = 70$ km s^{-1} Mpc^{-1}, $\Omega_M = 0.3$ and $\Omega_\Lambda = 0.7$ cosmology.

2 OBSERVATIONS OF THE Q2131−1207 FIELD

2.1 Quasar spectroscopy: absorption properties

The absorption system at $z_{abs} = 0.42980$ in the spectrum of the quasar Q2131−1207 was originally reported by Weymann et al. (1979) as a Mg II and Fe II absorber. Rao, Turnshek &
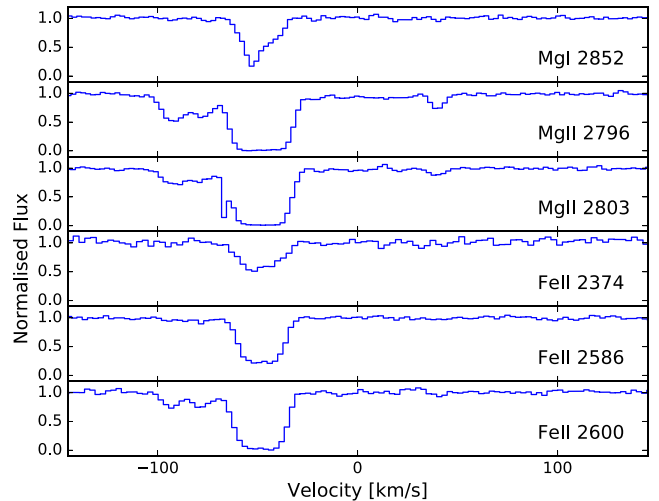

Figure 1. Absorption profiles. Excerpts from the high-resolution Keck/HIRES spectrum of the quasar Q2131−1207 showing absorption lines of Fe II, Mg II and Mg I. The zero velocity component is set to the redshift of galaxy 'a', $z_{gal} = 0.43005$. Most of the absorption appears to lie blue-wards of this systemic redshift. We note however one weak component at $\sim +50$ km s^{-1} which is only seen in the strongest transitions (i.e. Mg II).

Nestor (2006) measured $\log [N(\text{H I})/\text{cm}^{-2}] = 19.18 \pm 0.03$ from archival *Hubble Space Telescope* (*HST*)/Faint Object Spectrograph (FOS) spectra. Muzahid et al. (2016) used recent *HST*/ Cosmic Origins Spectrograph (COS) far-ultraviolet (FUV) data to derive $\log [N(\text{H I})/\text{cm}^{-2}] = 19.50 \pm 0.15$ which we adopt in the following.

Som et al. (2015) used *HST*/COS near-ultraviolet (NUV) spectroscopy to determine the absorption metallicity (S, Si and C) of the absorber using a five-component velocity structure over ~ 100 km s^{-1}. They further perform detailed photoionization modelling based on the CLOUDY software to estimate the ionization fraction of gas in this sub-DLA. Using the Si III/Si II ratio, they deduce an ionization parameter $\log U < -2.8$. The additional *HST*/COS FUV quasar spectra presented by Muzahid et al. (2016) confirm these results while providing additional information on the absorption properties of the system. Abundances of O, S, Si, C, N, Ar, Fe, Mg, Mn and Ca have been obtained from *HST*/COS for the first six elements and Keck/High Resolution Echelle Spectrometer (HIRES) archival spectra for the remaining (Som et al. 2015; Muzahid et al. 2016). Excerpts from the velocity profiles in Fe II, Mg II and Mg I are shown in Fig. 1. The zero velocity component is set to the redshift of galaxy 'a', $z_{gal} = 0.43005$. Most of the absorption appears to lie bluewards of this systemic redshift. We note however one weak component at $\sim +50$ km s^{-1} which is only seen in the strongest transitions (i.e. Mg II). The CLOUDY modelling by Muzahid et al. (2016) leads to a density of $\log (n_\text{H}/\text{cm}^{-2}) \sim -0.2$ corresponding to a density $n_\text{H} \sim 0.6$ cm^{-3} and an ionization parameter of $\log U \sim -5.6$ in agreement with earlier claims. The resulting ionization corrections vary from element to element, but are, as expected, negligible for O I, leading to an absorbing metallicity with respect to solar of $[\text{O/H}] = -0.26 \pm 0.19$ (1σ uncertainty).

Here, we apply the multi-element analysis proposed by Jenkins (2009) to estimate the dust content of the absorber. We refer the reader to Quiret et al. (2016) for a complete description of the method applied to quasar absorbers. In short, the method compares the dust depletion of dense neutral hydrogen systems to the
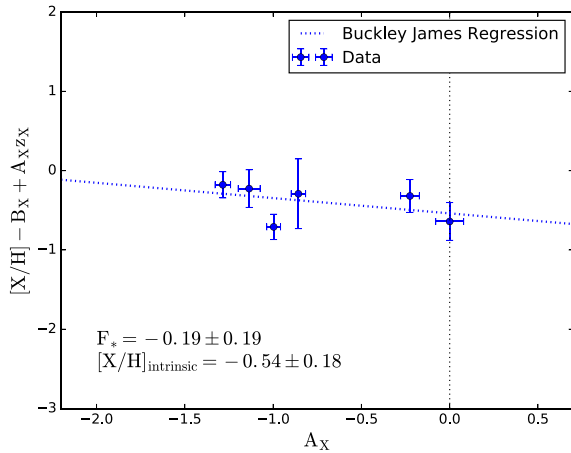
Figure 2. Multi-element analysis of the metallicity of the absorber. The method follows Quiret et al. (2016) and is based on the analysis developed by Jenkins (2009) to estimate the dust content of the absorber. The method compares the dust depletion of dense neutral hydrogen systems to that of the interstellar medium (ISM) of our Galaxy. The fit is represented by two parameters: F_* which is the line-of-sight depletion factor and A_x which is the propensity of the element X to increase the absolute value of its particular depletion level as F_* becomes larger. We find a F_* value of -0.19 ± 0.19 leading to a dust-free metallicity $[X/H] = -0.54 \pm 0.18$ (value at $A_x = 0$), corresponding to $12+\log(O/H) = 8.15 \pm 0.20$. This F_* value indicates a galaxy with low dust content, corresponding to a $\log A_V \sim -1.70$ (Vladilo et al. 2006).

gas-phase element abundances reported in the literature for 17 different elements sampled over 243 sightlines in the local part of our Galaxy. The trend of the depletions into solid form (dust grains) as a function of elements is characterized by two parameters: F_* which is the line-of-sight depletion factor and A_x which is the propensity of the element X to increase the absolute value of its particular depletion level as F_* becomes larger. We perform 100 000 realizations of the Buckley–James linear regression which treats limits using a survival analysis technique. In this case, we choose to exclude the C I upper limit because it appears to be inconsistent with the other measures. The determination of O I ($A_x = -0.225 \pm 0.053$) and N I ($A_x = -0.000 \pm 0.079$) column densities which have A_x values near zero means that the leverage on A_x is good as illustrated in Fig. 2. We find a F_* value of -0.19 ± 0.19 leading to a dust-free metallicity $[X/H] = -0.54 \pm 0.18$ (value at $A_x = 0$), corresponding to $12 + \log(O/H) = 8.15 \pm 0.20$ (using the solar value $12 + \log(O/H) = 8.69$ from Asplund et al. (2009)). This F_* value indicates a galaxy with low dust content, corresponding to an extinction $\log A_V \sim -1.70$ (Vladilo et al. 2006).

In addition, Muzahid et al. (2016) report the detection of molecular hydrogen in the absorber in one component at $z_{abs} = 0.42981$. This is at odds with findings from Ledoux, Petitjean & Srianand (2003) who report that absorbers with H_2 detections are usually
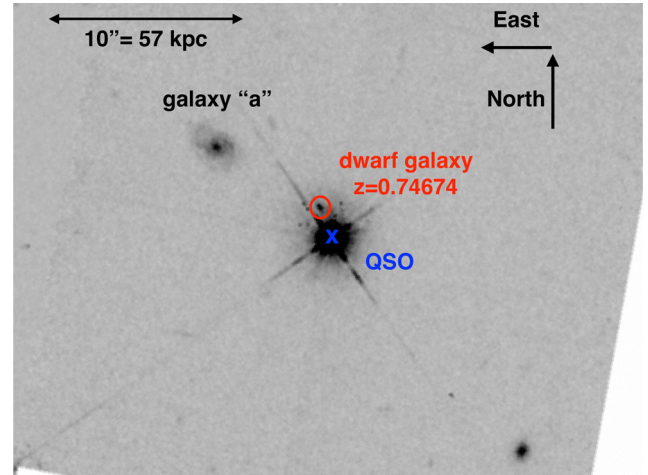
Figure 3. *HST*/WFPC2 F702 image of the quasar field. The quasar position is marked with a blue cross. Galaxy 'a' is clearly detected. The red circle shows the position of the dwarf galaxy at impact parameter $\delta = 2.06$ arcsec away from the quasar line-of-sight. The redshift is $z_{gal} = 0.74674$, i.e. higher than the redshift of the quasar. The MUSE spectrum of that object is shown in Fig. A1 of Appendix A.

amongst those having the largest depletion factors. Their fit results in a large total molecular fraction, $\log f_{H_2} = -2.84 \pm 0.17$. However, no absorption lines from $J > 3$ levels are observed possibly due to the absence of a local UV radiation field. A single excitation temperature can explain all of the remaining level populations, $T_{ex} = 206 \pm 6$ K, indicating the presence of cold gas. The authors note that the physical conditions in this system are similar to those of diffuse molecular clouds in the Galactic halo (Jenkins et al. 1973; Spitzer & Fitzpatrick 1995). The absorption properties of the sub-DLA are summarized in Table 1.

2.2 Imaging: a large galaxy

Bergeron (1986) discovered a galaxy located 8.6 arcsec away from the quasar from ground-based broad-band imaging. A spectrum confirms that the object is at the redshift of the absorber thanks to the detection of the [O II] doublet, $H\beta$, Ca H&K absorption doublet and a prominent break at the Balmer limit (see also Guillemin & Bergeron 1997). This was the first spectroscopic confirmation of a galaxy associated with a quasar absorber. Kacprzak et al. (2011) used *HST*/Wide Field and Planetary Camera 2 (WFPC2) *F702W* archival data shown in Fig. 3 and reported a *B*-band absolute magnitude $M_B = -20.32$ and a corresponding luminosity of $0.46L_*$. They further studied the morphological properties of the object using GIM2D modelling (Simard et al. 2002) and derived an inclination angle $\sin i = 0.75 \pm 0.05$ and half-light radius $r_{1/2} = 4.65$ kpc. Muzahid et al. (2016) used a Keck/ESI flux uncalibrated spectrum to report detections of $H\alpha$, [N II] and [O III] emission lines.

Table 1. Absorption properties of the sub-DLA towards Q2131−1207. The parameter $f_{H_2} = 2N(H_2)/[N(H I) + 2N(H_2)]$ indicates the molecular fraction in the absorber. The ionization parameter U is derived from the photoionization modelling. Here, we apply the multi-element analysis proposed by Jenkins (2009) to estimate the dust content of the absorber (Quiret et al. 2016). The derived value F_* indicates a galaxy with low dust content. The resulting metallicities and extinction are provided in the last columns of the table. The quoted errors are 1σ uncertainties.

Quasar field	z_{abs}	$\log N(H I)$ (cm^{-2})	$\log f_{H_2}$	$\log U$	F_*	$[X/H]_{dust-free}$	$12 + \log(O/H)$	$\log A_V$
Q2131−1207	0.42980	19.50 ± 0.15^a	-2.84 ± 0.17^a	-5.6^a	-0.19 ± 0.19^b	-0.54 ± 0.18^b	8.15 ± 0.20^b	-1.70^b

References: [a]Muzahid et al. (2016); [b]this work.

Table 2. Journal of MUSE observation of Q2131−1207.

Quasar field	Alternative name	RA	Dec.	z_{QSO}	B mag	V mag	R mag	T_{exp} (s)	Seeing (arcsec)
Q2131−1207	PHL 1598	21 31 35.26	−12 07 04.8	0.501	16.33	16.11	15.87	2×1200	0.72 ± 0.02

They used the first two lines to estimate an emission metallicity of $12 + \log(O/H) = 8.68 \pm 0.09$ from the N2 index (Pettini & Pagel 2004). They also argued, based on simple modelling, that the profiles of the absorption lines in the sub-DLA are inconsistent with those expected from a rotating disc associated with this galaxy, but the conclusion is heavily based on a mismatch in velocity space between the absorption profile and the rotation curve of the galaxy for which they derive an emission redshift $z_{gal} = 0.42966$.

Muzahid et al. (2016) note a dwarf galaxy nearer to the line-of-sight of the quasar (at impact parameter $\delta = 2.06$ arcsec, circled in red in Fig. 3) in the *HST* images and speculate it may be the source of H_2 absorption, although no spectroscopy was available at the time to confirm the redshift of that object. The object is also clearly detected in the MUSE data presented here and shows a number of strong emission lines including [O II], [Ne III], $H\delta$, $H\beta$, [O III] at $z_{gal} = 0.74674$, i.e. higher than the redshift of the quasar. A portion of the MUSE spectrum of that object is reproduced in Fig. A1 of Appendix A. This chance alignment once more calls for caution when associating absorbers with galaxies without spectroscopic information (Péroux et al. 2011a).

2.3 New MUSE observations

Although the absorbing galaxy was known prior to our observations, the MUSE field was centred on the quasar to maximize environmental studies. The observations were carried out in service mode (under programme ESO 96.A-0303 A) at the European Southern Observatory on the 8.2-m Yepun telescope. The seeing constraint for these observations was <0.8 arcsec and natural seeing mode was used. Two 'observing blocks' (OBs) were taken on the nights of 2015 October 4 and 8, respectively. The field was rotated by 90° between the two OBs. Each of these observations is 1200 s long. These were further divided into two equal subexposures, with an additional field rotation of 90° and subarcsec dithering offset in two-step pattern to minimize residuals from the slice pattern. The field of view is 59.9×60 arcsec², corresponding to a 0.2 arcsec pixel⁻¹ scale. We used the 'nominal mode' resulting in a spectral coverage of ∼4800–9300 Å. At the redshift of the target ($z \sim 0.4$), the data cover emission lines from [O II]$\lambda\lambda3727$, 3729to [O III] $\lambda5008$. The spectral resolution is $R = 1770$ at 4800 Å and $R = 3590$ at 9300 Å resampled to a spectral sampling of 1.25 Å pixel⁻¹. A journal of observations summarizing the properties of the targeted quasar is presented in Table 2.

The data were reduced with version v1.6 of the ESO MUSE pipeline (Weilbacher 2015) and additional external routines for sky subtraction and extraction of the 1D spectra. Master bias, flat-field images and arc lamp exposures based on data taken closest in time to the science frames were used to correct each raw cube. We checked that the flat-fields are the closest possible to the science observations in terms of ambient temperature to minimize spatial shifts. In all cases, we found the temperature difference to be less than 0°.27, below the canonical 0°.5 set to be the acceptable limit. Bias and flat-field correction are part of the ESO pipeline. The raw science data were then processed with the SCIBASIC and SCIPOST recipes. During this step, the wavelength calibration was corrected to a heliocentric

reference. We checked the wavelength solution using the known wavelengths of the night-sky OH lines and found it to be accurate within 25 km s⁻¹. The individual exposures were registered using the point sources in the field within the EXP_ALIGN recipe, ensuring accurate relative astrometry. Finally, the individual exposures were combined into a single data cube using the EXP_COMBINE recipe. The seeing of the final combined data is measured from the quasar and other bright point source in the data cube. The resulting point spread function (PSF) has a full width at half-maximum of 0.72 ± 0.02 arcsec at 7000 Å.

The removal of OH emission lines from the night sky is accomplished with additional purpose-developed codes using two different methods. The SCIPOST recipe is first performed with sky-removal method turned off. The sky subtraction is then done with the Zurich Atmosphere Purge (ZAP) code (Soto et al. 2016). After masking bright objects in the field, ZAP uses a principal component analysis (PCA) to isolate the residual sky subtraction features and remove them from the observed data cube. In the second pass, the SCIPOST recipe is run with the sky subtraction method 'simple' on, which directly subtracts a sky spectrum created from the data, without regard to the line spread function (LSF) variations. Again, after selecting sky regions in the field, we create PCA components from the spectra which are further applied to the science data cube to remove sky line residuals (Husemann et al. 2016). This second method is found to significantly improve the sky subtraction over large parts of the MUSE field-of-view and is chosen to process the data presented here.

The resulting flux calibration is compared with the R magnitudes of three known objects in the field, including the quasar itself, in order to estimate the flux uncertainties. The MUSE spectra of these objects are extracted and their broad-band fluxes are computed using an R filter passband. These fluxes are computed as AB magnitudes directly using the following relation:

$$AB = -2.5\log_{10}(F_\lambda) - 5\log_{10}(\langle\lambda\rangle) - 2.406, \tag{1}$$

where F is the flux in erg s⁻¹ cm⁻² Å⁻¹ and $\langle\lambda\rangle$ the filter central wavelength in Å. The differences are found to be small (0.07 mag) and the mean of the differences of three reference objects provides an estimate on the flux error of ±12 per cent.

3 ANALYSIS

3.1 Galaxy detections

Fig. 4 presents the reconstructed white-light image of the combined exposures. All the objects identified in the field are marked with a black or white square with an associated id number. Fig. 5 presents a pseudo-narrow-band filter around [O III] $\lambda5008$ at the redshift of the absorber. The PSFs of the bright objects in the field are removed and marked with black crosses but for the quasar which is shown as a blue cross. Fig. 6 is a 3D rendering of the same narrow wavelength slice of the cube. One object appears to be coincident with the redshifted wavelength of [O III] $\lambda5008$ at the redshift of the sub-DLA. However, the emission line is undoubtedly Lyα from a galaxy at $z_{gal} = 4.8986$, as indicated by the characteristic
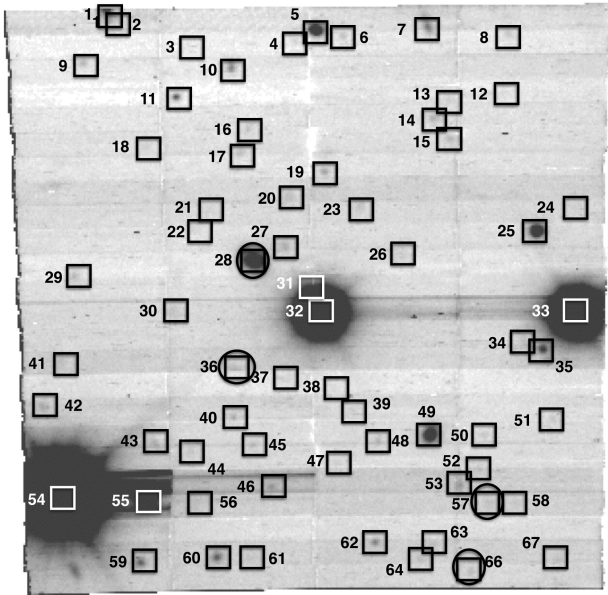
Figure 4. Reconstructed white-light image of the combined exposures. Orientation is north(up)-east(left) and the field-of-view is 59.9×60 arcsec^2. All the objects identified in the field are marked with a black or white (colour depending on contrast) square with an associated id number. The quasar is object 32, the nearby dwarf galaxy at $z_{gal} = 0.74674$ is object 31 and the strong emitter at $z_{gal} = 4.8986$, coincident with the redshifted wavelength of [O III] $\lambda5008$ at the redshift of the sub-DLA is object 38. Objects 28, 36, 57 and 66 shown with an additional circle have redshifts consistent with the absorption redshift of the sub-DLA present in the quasar spectrum.

asymmetric emission+absorption line profile and the presence of narrow N V $\lambda1240.81$ emission (Fig. A2 of Appendix A). This object is marked as 'LAE' in Fig. 5 and shown with a red arrow in Fig. 6.

In these MUSE data, we recover the known large galaxy (galaxy 'a') reported by Bergeron (1986) at an angular distance of 9.2 arcsec from the quasar. This bright object is clearly extended and displays
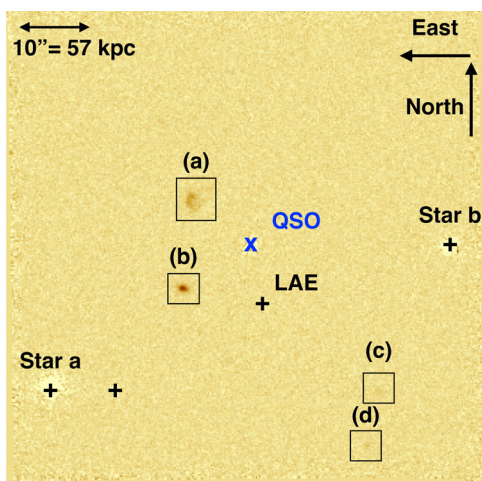
Figure 5. A pseudo-narrow-band filter around [O III] $\lambda5008$ at the redshift of the absorber. The PSF of the bright objects in the field are removed and marked with black crosses but for the quasar which is shown as a blue cross. The spectrum of the object labelled Lyα emitter (LAE) is shown in Fig. A2 of Appendix A. The four emitters at the redshift of the sub-DLA are shown with squares and labelled 'a' to 'd'. These are the same objects as labelled 28, 36, 57 and 66 in Fig. 4.
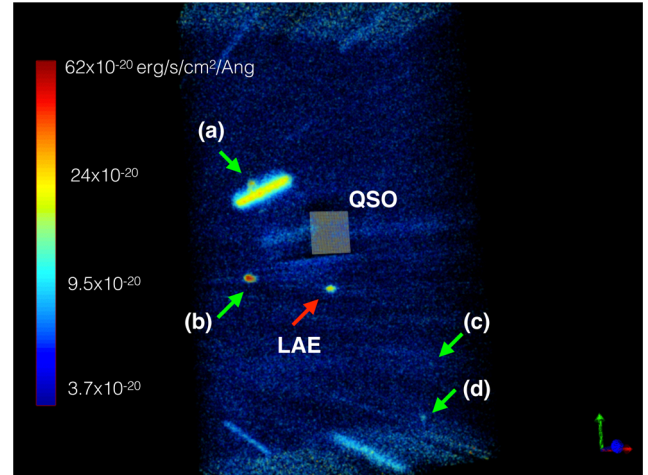
Figure 6. A 3D rendering of the pseudo-narrow-band filter around [O III] $\lambda5008$ at the redshift of the absorber. The colour bar indicates fluxes in units of 10^{-20} erg s^{-1} cm^{-2} Å^{-1}. Orientation is north(up)-east(left). Continuum-detected objects are shown as cylinders. The quasar has been subtracted and its location is shown as a grid in the wavelength plane. The emitters at the redshift of the sub-DLA are indicated with green arrows. The northern most object is clearly detected in the continuum while others are not. The red arrow indicates a background Lyα emitter at $z_{gal} = 4.8986$, whose spectrum is shown in Fig. A2 of Appendix A.

spiral arms or possibly tidal tails from an interacting system. In addition to this object, we report three new detections at the redshift of the sub-DLA. One of these, dubbed galaxy 'b' is at a similar angular distance from the quasar as galaxy 'a', 10.7 arcsec. It is significantly fainter than galaxy 'a' and barely visible in the *HST* images (Muzahid et al. 2016). Two other objects, galaxies 'c' and 'd' are further away at 26.0 and 30.7 arcsec, respectively, corresponding to 147 and 174 kpc at the redshift of the sub-DLA and fall outside the *HST* field. While we consider these two galaxies to be too far away from the quasar sightline to be the hosts of the sub-DLAs (Péroux et al. 2003), they are likely to trace a more general structure at that redshift. The sky location of each of these objects is reported in Table 3, including a reference id from Fig. 4.

To extract 1D spectra for each of these galaxies, we adjust the radius according to the galaxy size to be (for galaxy 'a' to 'd'): 10, 5, 3 and 8 pixels, respectively, and add the 1D spectra for each spaxel within these radii. Fig. 7 presents the resulting whole spectrum for galaxy 'a'. The continuum of galaxy 'a' is clearly detected, showing also numerous emission lines of the unresolved [O II] doublet, Hδ, Hβ and [O III] as well as absorption lines from Ca H&K and a prominent Balmer decrement. We note that the absorption lines from Ca H&K aligned well with the systemic redshift of the galaxy so that he 'down-the-barel' technique indicates no sign of gas flows at this spectral resolution. The remaining galaxies have a weak continuum but all show the five emission lines listed above, except for galaxy 'c' for which an upper limit in [O III] 4960 Å can be derived and galaxy 'd' for which an upper limit in [O III] 5008 Å can be derived. We derive a 3σ upper limit for non-detection based on the measured rms at the expected position of the line for an unresolved source spread over 6 spatial pixels and spectral FWHM = 2.4 pixels = 3 Å. Fig. 8 displays the [O II] (left-hand panel) and Hβ and [O III] (right-hand panel) regions of all four galaxies.

The fluxes of the detected emission lines are estimated from Gaussian fit. The Hβ emission line in galaxy 'a' has the characteristic broad stellar absorption line component at the base of the

Table 3. Sky location of the four objects at the redshift of the absorber. Sky offsets are relative to the central position of the quasar. δ is the angular distance in arcsec and the impact parameter in kpc. The redshift of the strongest component of the absorption profile is $z_{abs} = 0.42980$. The broad-band R magnitudes and luminosity relative to L_* are also provided.

Galaxy	Id Fig. 4	ΔRA (arcsec)	ΔDec. (arcsec)	δ (arcsec)	δ (kpc)	z_{gal}	M_R	L/L_*	Reference
Galaxy a	28	+7.2	+5.7	9.2	52	0.43005	−21.16	0.60	Bergeron 1986; this work
Galaxy b	36	+8.9	−5.9	10.7	61	0.43072	−19.70	0.15	This work
Galaxy c	57	−17.2	−19.5	26.0	147	0.43006	−16.38	0.01	This work
Galaxy d	66	−15.5	−26.4	30.7	174	0.42982	−16.25	0.01	This work
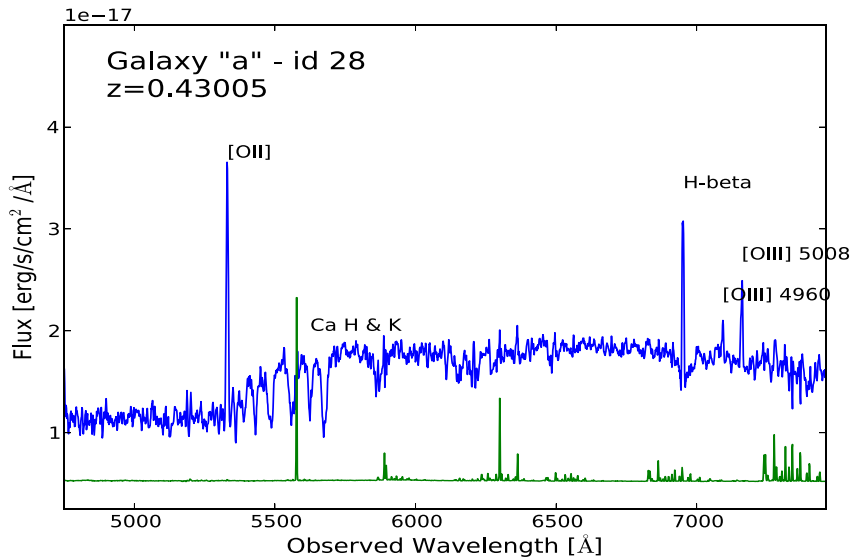
Figure 7. MUSE spectrum of galaxy 'a'. In this and the following figure, the MUSE spectrum is shown in blue and the sky spectrum is shown in green (not to scale and arbitrarily offset). The flux scales are indicated above the top left-hand corner of the panel. The object lies $\delta = 9.2$ arcsec (52 kpc) away from the quasar line-of-sight at $z_{gal} = 0.43005$. The spectrum is smoothed (3-pixel boxcar) for display purpose. The continuum is clearly detected, showing also numerous emission lines of the unresolved [O II] doublet, Hδ, Hβ and [O III] as well as absorption lines from Ca H&K and a prominent Balmer decrement. Some other absorption lines are due to tellurics.
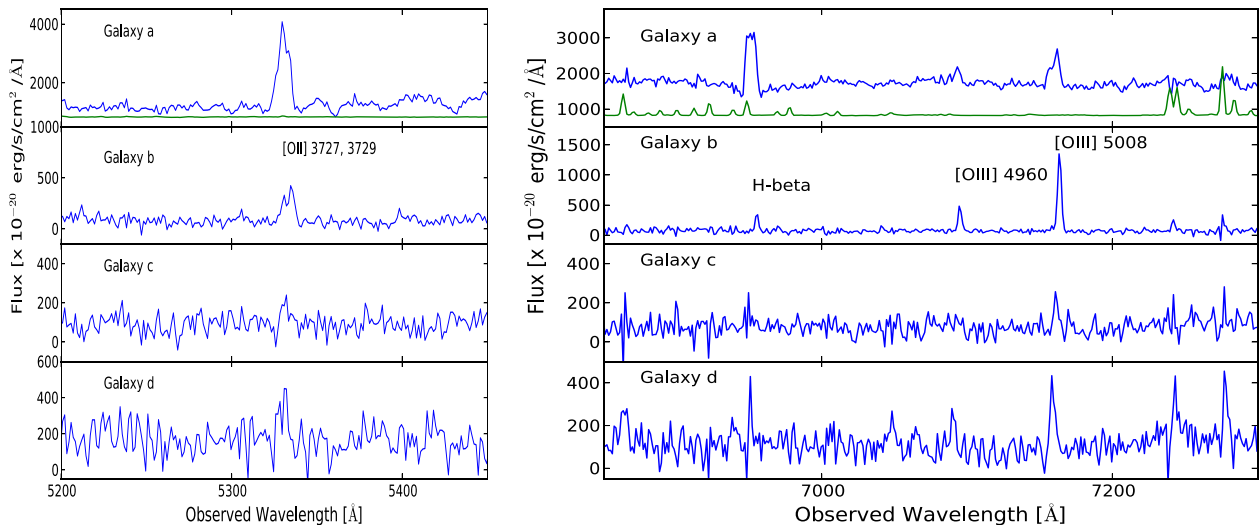
Figure 8. MUSE spectra of galaxies 'a' to 'd'. The [O II] (left-hand panel) and Hβ and [O III] (right-hand panel) regions of all four galaxies are shown. The four objects have redshifts consistent with that of the quasar absorber.

emission line which we have removed before fitting the emission line itself (Zych et al. 2007). We do not correct the emission lines fluxes for reddening because Hα is not covered by our data and Hγ is too weak. In addition, we use the fit of four of the emission lines

(namely the [O II] doublet, Hβ, [O III] λ4960 and [O III] λ5008) to estimate the redshifts of the emitting galaxies. For galaxy 'a', we derive $z_{gal} = 0.43005$ also including Hδ from the MUSE spectrum calibrated in air. This value of z_{gal} is at odds with the earlier

Table 4. Physical properties of the detected galaxies. The fluxes are expressed in erg s^{-1} cm^{-2}. The redshifts are determined from the 1D MUSE spectra calibrated in air. The SFR is estimated from [O II] fluxes without dust correction. The metallicity is based on the R_{23} index. For comparison, the metallicity of the neutral gas probed in absorption is $12 + \log(O/H) = 8.15 \pm 0.20$. The quoted errors are 1σ uncertainties.

Galaxy	F([O II]) (erg s^{-1} cm^{-2})	F(Hβ) (erg s^{-1} cm^{-2})	F([O III]) 4960 (erg s^{-1} cm^{-2})	F([O III]) 5008 (erg s^{-1} cm^{-2})	SFR (M$_\odot$ yr^{-1})	$12 + \log(O/H)$
Galaxy a	$21.4 \pm 2.1 \times 10^{-17}$	$16.3 \pm 1.6 \times 10^{-17}$	$2.2 \pm 0.2 \times 10^{-17}$	$6.7 \pm 0.7 \times 10^{-17}$	2.0 ± 0.2	8.98 ± 0.02
Galaxy b	$2.4 \pm 0.2 \times 10^{-17}$	$0.8 \pm 0.1 \times 10^{-17}$	$1.2 \pm 0.2 \times 10^{-17}$	$4.2 \pm 0.4 \times 10^{-17}$	0.2 ± 0.1	8.32 ± 0.16
Galaxy c	$0.8 \pm 0.1 \times 10^{-17}$	$0.2 \pm 0.1 \times 10^{-17}$	$<0.6 \times 10^{-17}$	$0.6 \pm 0.1 \times 10^{-17}$	0.08 ± 0.1	–
Galaxy d	$1.5 \pm 0.1 \times 10^{-17}$	$0.5 \pm 0.1 \times 10^{-17}$	$0.7 \pm 0.1 \times 10^{-17}$	$<1.2 \times 10^{-17}$	0.1 ± 0.1	–

Note. The 3σ upper limit for non-detection is computed for an unresolved source spread over 6 spatial pixels and spectral FWHM = 2.4 pixels = 3 Å.

measure by Muzahid et al. (2016) who reported $z_{gal} = 0.42966$. We note that the dispersion between the measurements of the different lines is $\Delta z = 0.00033$, corresponding to $\Delta v = 70\,\mathrm{km\,s^{-1}}$. The physical properties of the four galaxies deduced from the emission line fits are collected in Table 3. We find that the maximum redshift difference between these objects, $\Delta z = 0.00090$, which translates into a velocity difference of only $\Delta v \simeq 200\,\mathrm{km\,s^{-1}}$, significantly above our wavelength calibration accuracy ($25\,\mathrm{km\,s^{-1}}$). Finally, we build a MUSE cube with the Cousins R filter band-pass to compute the broad-band R magnitude and luminosities relative to L_* (Lin et al. 1996) as listed in Table 3.

3.2 Star formation rates

Based on the [O II] detections, we derive the star formation rate (SFR) using the prescription by Kennicutt (1998):

$$\mathrm{SFR}_{[O II]} = (1.4 \pm 0.4) \times 10^{-41} L([O II]). \tag{2}$$

We note that the [O II] doublet at the redshift of the sub-DLA is slightly affected by a weak sky line which happens to fall right in between the two lines of the doublet. The resulting SFRs, uncorrected for dust depletion, are listed in Table 4. Galaxies 'a' and 'b' with SFR $\geq 0.2\,\mathrm{M_\odot\,yr^{-1}}$ are star-forming galaxies while galaxies 'c' and 'd' are passive (Rauch et al. 2008).

3.3 Metallicity

Emission lines are commonly used to estimate gas-phase metallicities in extragalactic H II regions. We use the R_{23} indicator which was first introduced by Pagel et al. (1979), and is widely used for measuring the oxygen abundances if the fluxes of [O III] and [O II] are known:

$$\log R_{23} = \log \left(\frac{[O II]\lambda\lambda 3727, 3729 + [O III]\lambda\lambda 4960, 5008}{H\beta} \right). \tag{3}$$

The resulting metallicities are derived using the relation of Mc-Gaugh (1991) which accounts for the level of ionization via the O32 parameter (see Kobulnicky, Kennicutt & Pizagno 1999 for the relevant equations). The resulting values are listed in Table 4. For galaxy 'a', we use the metallicity derived from the N2-index indicator of Pettini & Pagel (2004) to exclude the lower branch. We note that for that object, our estimate of the metallicity ($12 + \log(O/H) = 8.98 \pm 0.02$) is higher than the one reported by Muzahid et al. (2016): $12 + \log(O/H) = 8.68 \pm 0.09$; which can be explained by the fact that they use the N2-index which is known to saturate at solar metallicities (Pettini & Pagel 2004). Thus, the R_{23} index is probably

more reliable in this regime.[1] We also note that both these values are higher than the metallicity of the neutral gas probed in absorption reported in the earlier section: $12 + \log(O/H) = 8.15 \pm 0.20$ (see Table 1). For galaxy 'b', we derive $12 + \log(O/H) = 8.32 \pm 0.16$, i.e. a value consistent with the absorption metallicity within the errors. We cannot put stringent constraints on the metallicity estimates of galaxy 'c' and 'd'.

In addition, for galaxy 'a', we have been able to derive the metallicity gradient inside the galaxy based on two measures of the metallicity (centrally in a 3-pixel radius and in annulus around it). We measure a slope $+0.01 \pm 0.03$ dex kpc^{-1} consistent with a flat distribution of metallicities. We recall, that for the local galaxy gradients, the isolated spiral control sample of Rupke, Kewley & Chien (2010) indicates a median slope of -0.041 ± 0.009 dex kpc^{-1}. These two values are consistent within the errors. Extrapolating the slope of $+0.01 \pm 0.03$ dex kpc^{-1} to the impact parameter of galaxy 'a' (52 kpc) would lead to an expected metallicity $12 + \log(O/H) = 9.36 \pm 1.56$ which is consistent with the one measured in absorption: $12 + \log(O/H) = 8.15 \pm 0.20$. We warn the reader, however, that these two metallicity indicators provide a measure of the metallicity in different phases of the gas (Péroux et al. 2012; Rahmani et al. 2016).

3.4 Morphological and kinematical properties

To estimate the kinematics of the galaxies, we use two different algorithms. First, we use the CAMEL code (Epinat et al. 2009) which fits simultaneously several emission lines in the presence of a continuum. In this case, we fit Hβ and doublets from [O II] and [O III] simultaneously. In the case of galaxy 'a', the continuum contribution comes from the galaxy continuum and the nearby quasar continuum. Second, we use the GALPAK^{3D} algorithm (Bouché et al. 2015) which compares directly the data cube with a parametric model mapped in x, y, λ coordinates. The algorithm uses a Markov chain Monte Carlo (MCMC) approach with a non-traditional proposal distribution of the parameters in order to efficiently probe the parameter space. The code has the advantages that it fits the galaxy in 3D space and provides a robust description of the morphokinematics of the data even in poor seeing conditions. We set the input parameters and model profiles and compare them with the actual data so as to obtain a convergence of the 10 free parameters (sky position, flux, half-light radius, inclination, PA, turnover radius, maximum velocity and velocity dispersion) over a 15 000 long MCMC in order to robustly sample the posterior probability distribution. Details of the method can be found in Bouché et al. (2015).

---

[1] Although we note that since we have not applied any dust extinction correction to the measured emission line fluxes, our value of $12 + \log(O/H)$ for galaxy 'a' may be an overestimate.

Table 5. Galaxy 'a' morphokinematic properties. These morphological and kinematic parameters are determined from our 3D fits using the GALPAK^{3D} algorithm. They are all corrected for inclination. PA stands for position angle. The azimuthal angle is the angle between the quasar line-of-sight and the projected major axis of the galaxy on the sky. The galaxy is inclined and presents all characteristics of a rotating disc.

	$r_{1/2}$ (kpc)	$\sin i$	PA (°)	Azimuthal angle (°)	V_{max} (km s^{-1})	M_{dyn} (M$_\odot$)	M_{halo} (M$_\odot$)
Galaxy a	7.9 ± 0.1	0.87 ± 0.01	65 ± 1	12 ± 1	200 ± 3	$7.4 \pm 0.4 \times 10^{10}$	$2.9 \pm 0.2 \times 10^{12}$

The code provides stable results given certain conditions. First of all, the signal-to-noise ratio (S/N) per spaxel of the brightest spaxel should be >3. For Galaxy 'a', the S/N per spaxel of the brightest pixel in the Hβ cube is 4.3. For Galaxy 'b', it is only ~2. Indeed, GALPAK^{3D} does not converge for galaxy 'b' in part because the object is compact and also because the S/N per spaxel of the brightest spaxel is below the stability criterion for the algorithm convergence. Similarly, galaxies 'c' and 'd' are too faint ($L/L_* \sim 0.01$) and compact to perform a robust morphokinematics analysis. Second, Bouché et al. (2015) note that the algorithm performs well if the half-light radius is such that $r_{1/2}$/FWHM > 0.75, which in our case (FWHM = 0.72 arcsec) translates into $r_{1/2}$ > 0.54 arcsec or $r_{1/2}$ > 2.7 pixel (0.2 arcsec pixel scale). We check that the $r_{1/2}$ value derived by the model satisfies this condition. Third, we examined the covariance between the fitted parameters to check that potential degeneracies are broken (typically between V_{max} and inclination i and V_{max} and turnover radius r_v). To overcome the covariance between r_v and V_{max}, we set the turnover radius r_v to satisfy the scaling relation between r_v and the disc exponential R_d found in local disc samples, which is approximately $r_t \simeq R_d \times 0.9$. In practice, we fixed r_v to 1.5 kpc (i.e. ~1.3 spaxel). Fourth, we aim at an acceptance rate (fraction of useful iterations count to total iterations count) of the MCMC between 30 and 50 per cent. In the case of galaxy 'a', we need to adjust the maximum number of accepted iterations (RANDOM_SCALE) to reach such values of acceptance rate. Finally, we examined the residual maps to make sure that no significant features are present after the model is subtracted from the data. We use the default exponential flux profile but note that using a Gaussian flux profile does not affect the results. In all cases, we use an arctan velocity profile which best represents the data.

The [O III] λ4960 line was not used, but [O III] λ5008 Å and Hβ were fitted independently and the resulting fit parameters agree very well within the error estimates. We find that the maximum circular velocity is well constrained at around $V_{max} = 200 \pm 3$ km s^{-1}. The half-light radius converges at about 7.9 ± 0.1 kpc, and the position angle (PA) is found to be $65° \pm 1°$. The inclination is $\sin i = 0.87 \pm 0.01$, i.e. slightly higher than the one reported by Kacprzak et al. (2011) from a GIM2D modelling of *HST* observations ($\sin i = 0.75 \pm 0.05$). These results are collected in Table 5.

The morphological analysis indicates the presence of spiral arms or possibly tidal tails in an interacting system as well as substructure in [O III] on scales of 1 arcsec. The galaxy has a large inclination angle. Both the observed and model velocity maps indicate a gradient along the major axis of the galaxy. In addition, the dispersion peaks in the centre of the object. All these characteristics point to a large rotating disc. We note that the kinematic model from Muzahid et al. (2016) would also be consistent with rotation had they used the redshift measured here $z_{gal} = 0.43005$. Indeed, our measure is probably more reliable as it is based on several high S/N emission lines while they have access to a rather noisy spectrum covering only Hα and [N II] lines. Fig. 9 shows the resulting [O III] flux and velocity maps, where the direction to the quasar is indicated with a white arrow. The maps in the bottom row of Fig. 9 illustrate the

results from our 3D modelling. The model is a good representation of the data, which can be appreciated from the residuals from the subtraction of the model from the observations shown in bottom right-hand panel.

Given that galaxy 'a' is rotating, we can use the enclosed mass to determine the dynamical mass within $r_{1/2}$ (Epinat et al. 2009):

$$M_{dyn} = V_{max}^2 r_{1/2}/G, \qquad (4)$$

where V_{max} and $r_{1/2}$ are measured from kinematic analysis above and are corrected for inclination. We therefore find $M_{dyn} = 7.4 \pm 0.4 \times 10^{10}$ M$_\odot$.

We are able to estimate the mass of the halo in which the systems reside, assuming a spherical virialized collapse model (Mo & White 2002):

$$M_{halo} = 0.1 H_0^{-1} G^{-1} \Omega_m^{-0.5} (1 + z)^{-1.5} V_{max}^3, \qquad (5)$$

using the V_{max} value. We find $M_{halo} = 2.9 \pm 0.2 \times 10^{12}$ M$_\odot$ for galaxy 'a'. These results are listed in Table 5.

The top row of Fig. 10 presents the [O III] flux map, observed velocity and velocity dispersion maps of galaxy 'b'. Although the object is compact, there are no indications of rotation from velocity and dispersion maps. Galaxies 'c' and 'd' [O III] flux maps are shown at the bottom of Fig. 10.

4 NATURE OF THE GAS

In this study, we are able to combine information on the properties of neutral gas seen in absorption in front of the quasar Q2131$-$1207 with the wealth of data provided by MUSE on a group of galaxies at the same redshift as the absorber, including impact parameters, SFRs, metallicities, morphological and kinematic properties. In the following, we review possible scenarios to explain the relation between the gas seen in absorption and the four galaxies we have identified. However, we consider galaxies 'c' and 'd' to be too far away from the quasar sightline (at 26.0 and 30.7 arcsec, respectively, corresponding to 147 and 174 kpc at the redshift of the sub-DLA) to be *directly* associated with the gas observed in absorption (see e.g. Péroux et al. 2005; Rubin et al. 2015 for an estimate of the size of quasar absorbers).

4.1 Gas rotating with the disc

Based on the observed velocity and dispersion maps (see Fig. 10), galaxy 'b' does not show signs of rotation nor other significant velocity gradients. This could partly be an effect of beam smearing in natural seeing observations, limiting our ability to discern rotation in galaxy 'b'. In addition, it is slightly further away (61 kpc) than galaxy 'a' (52 kpc) and with a larger velocity offset ($z_{gal} = 0.43072$) from the main component of the absorber, $z_{abs} = 0.42980$. For these reasons, we explore the possibility that the gas seen in absorption is related to the gas in rotation around galaxy 'a', which lies at $z_{gal} = 0.43005$. In that object, we measure $V_{max} = 200 \pm 3$ km s^{-1} with the blueshifted side of the galaxy oriented towards the quasar
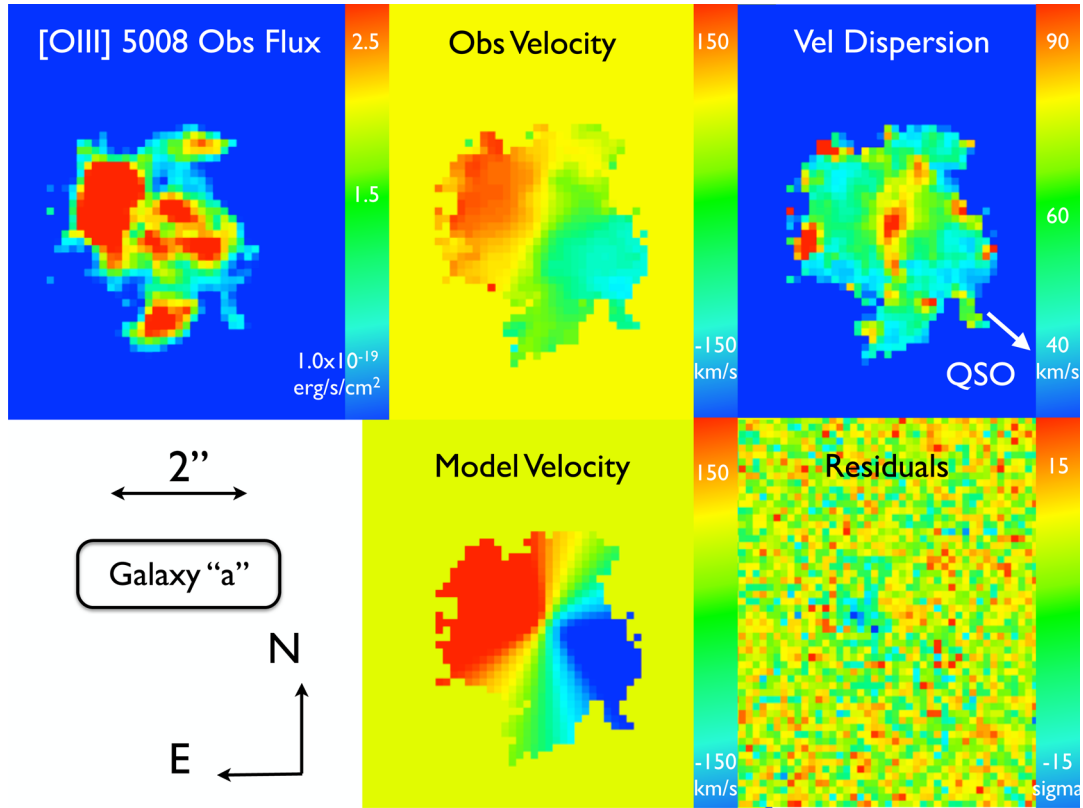
Figure 9. Morphokinematic analysis of galaxy 'a'. The maps in the top row show the MUSE observations. The maps in the bottom row illustrate the results from our 3D modelling. The bottom right-hand panel shows the residuals from the subtraction of the model from the observations. The direction to the quasar is shown with a white arrow in the top right-hand panel. The orientation and scales are indicated on the figures. The maps clearly show the spiral arms of galaxy 'a' or possibly tidal tails in an interacting system as well as substructure in [O III] on scales of 1 arcsec. The velocity field and velocity dispersion (peaking in the centre) maps clearly indicate rotation expected from an extended disc. We measure $V_{\text{max}} = 200 \pm 3 \, \text{km s}^{-1}$ corresponding to $M_{\text{dyn}} = 7.4 \pm 0.4 \times 10^{10} \, \text{M}_\odot$ and $M_{\text{halo}} = 2.9 \pm 0.2 \times 10^{12} \, \text{M}_\odot$.

line-of-sight (see Fig. 9). This is broadly consistent with what is seen in the absorption profile, with most of the absorption taking place at velocities between $v \simeq -100$ and $-50 \, \text{km s}^{-1}$ from the systemic redshift of galaxy 'a' (see Fig. 9). In addition, the metallicity measured in absorption is comparable with the one expected from the measured flat internal metallicity gradient at impact parameter $\delta = 52$ kpc. However, we note that this scenario does not explain the weak components seen in absorption in the strong lines of Mg II and redwards of the systemic redshift of the galaxy at $v \simeq +50 \, \text{km s}^{-1}$. This further calls for additional physical processes to explain the gas seen in absorption.

4.2 Gas flows

Simulations indicate that in galaxies driving large-scale outflows the outflowing gas preferentially leaves the galaxy along its minor axis (path of least resistance), preventing infall of material from regions above and below the disc plane (Brook et al. 2011). As a result, inflowing gas is almost coplanar with the galaxy disc and is seen preferentially along the major axis (Bordoloi et al. 2011; Stewart et al. 2011; Shen et al. 2012). Thus, information on orientation potentially allows one to observationally distinguish winds from accreting gas (e.g. Péroux et al. 2013; Schroetter et al. 2015).

Because it is compact, we cannot constrain the inclination of galaxy 'b', which prevents us from measuring its azimuthal angle. For galaxy 'a', we measure of the azimuthal angle between

the quasar line-of-sight and the projected major axis of the galaxy on the sky. We find the azimuthal angle to be $12° \pm 1°$, which would exclude the outflow scenario. This is further supported by the fact that the integrated metallicity of the galaxy, $12 + \log(\text{O/H}) = 8.98 \pm 0.02$, is higher than the metallicity of the absorbing gas, $12 + \log(\text{O/H}) = 8.15 \pm 0.20$.

On the contrary, based on geometry and orientation arguments, it is possible that the gas seen in absorption is related to infalling cold gas on to galaxy 'a'. This is further supported by the metallicity difference between the galaxy and the sub-DLA absorber. The object lies in the infalling part of the galaxy to gas metallicity difference versus azimuthal angle plot proposed by Péroux et al. (2016). However, with the present data, we cannot exclude that the gas is possibly (or also) infalling on to galaxy 'b'.

4.3 Intragroup gas

Galaxies 'c' and 'd' are too far away from the quasar line-of-sight at 147 and 174 kpc, respectively, to be directly associated with the absorber and play a direct role in the possible scenarios above. However, their presence indicates that they are likely to trace a more general structure at that redshift. Given the separation between the galaxies which are the furthest apart in velocity space (galaxies 'b' and 'd'), we calculate that our observations probed a volume of 0.694 Mpc^3 at the redshift of the absorber. We use the luminosity function at this redshift reported by Cowie, Barger & Hu (2010) to
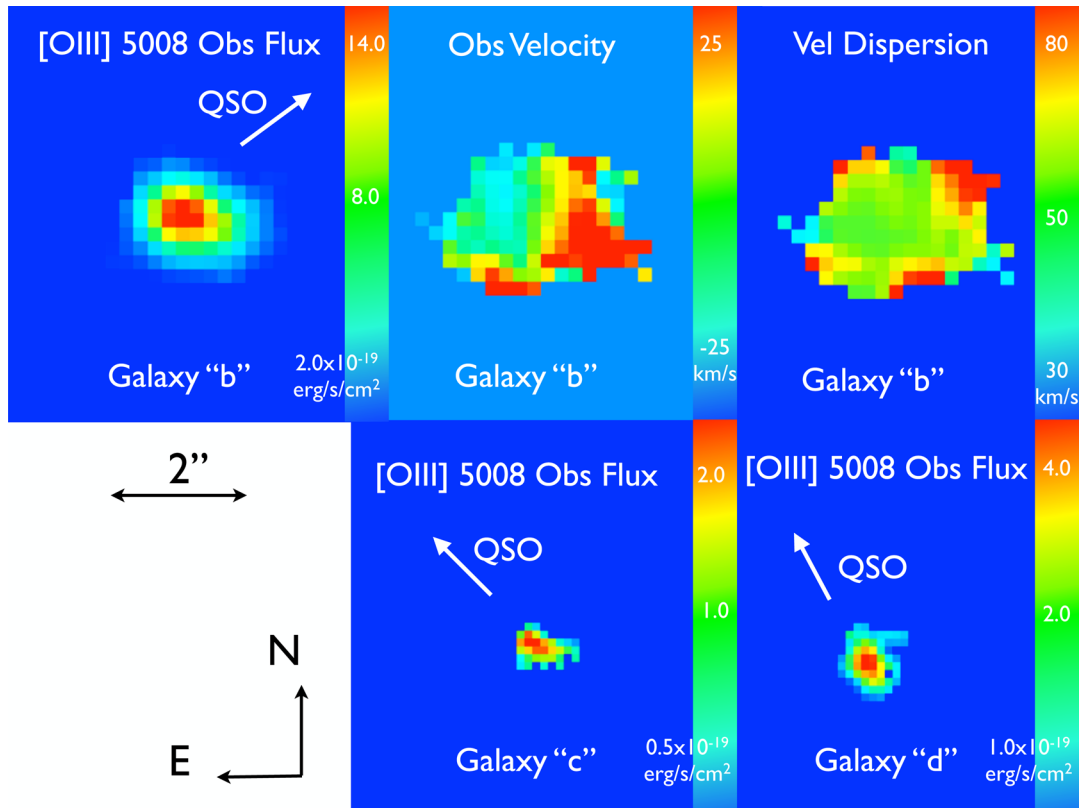
Figure 10. Observed flux maps of galaxies 'b', 'c' and 'd'. The top row shows the [O III] flux map, observed velocity map and dispersion map of galaxy 'b'. Although the object is compact, there are no indications of rotation from velocity and dispersion maps. Galaxies 'c' and 'd' [O III] flux maps are shown at the bottom. In all flux panels, the direction to the quasar is shown with a white arrow.

estimate that only 0.02 galaxies should be expected above our sensitivity limit (see also Deharveng et al. 2008 for the determination of the low-redshift luminosity function). Therefore, the four objects detected represent a significant overdensity.

The two closest objects (galaxies 'a' and 'b') are $\delta = 11.3$ arcsec (64 kpc) apart which means that they could be interacting, possibly tidally stripping. Given that the distance between the two objects with the largest separation on the plane of the sky (galaxies 'a' and 'd') is ~200 kpc, the data at hand point to a group scale structure. However, the lack of information on larger scales prevents us from excluding a cluster. The velocity dispersion of the four objects is $81\,\mathrm{km\,s^{-1}}$ which is in the range of small galaxy groups. Based on such dispersion and assuming a virialized spherical system, we obtain a virial radius of 200 kpc. The virial mass for such system will be $3.3 \times 10^{11}\,\mathrm{M_\odot}$. This value is an order of magnitude lower than the halo mass for galaxy 'a': $M_{\mathrm{halo}} = 2.9 \pm 0.2 \times 10^{12}\,\mathrm{M_\odot}$. However, the virial mass of the halo should be considered as a lower limit, since we may not have seen all group members, leading to underestimates of the dispersion and virial radius. In addition, we note the possible alignments of the objects in what could be a filament with a north-east to south-west orientation (Møller & Fynbo 2001; Fumagalli et al. 2016).

5 DISCUSSION

The large amount of data gathered in this work allows us to put constraints on possible scenarios explaining the origin of the gas seen in absorption. We find that part of the absorption profile can be explained by the rotating disc of galaxy 'a'. We exclude the

possibility that the absorption is due to outflows but favour a scenario where some of the gas is infalling on to galaxy 'a' and/or 'b'. Additionally, we argue that some gas may be related to the larger structure (group or filament) traced by the presence of four galaxies at the redshift of the absorber. We further note that several of these scenarios in combination might explain the final absorption profile. It is likely that neutral gas probed in absorption is related in part to gas bound to a large object in a group and/or filament and in part to intragroup gas. If that is the case, one can then question whether the physical properties of the main member of the group are a good representation of the galaxy properties seen in absorption, regardless of the exact identification of the absorbing gas.

These results have several implications. First of all, this case and others (Bielby et al. 2016; Fumagalli et al. 2016) challenge a possibly oversimplified picture where gas can be associated with a single isolated object and gas flow directions can be solely determined from geometry and orientation considerations. Indeed, this approach needs to be combined with information on the metallicity of the gas which is key to a complete understanding of gas flows. Only by selecting absorbers with measured $N(\mathrm{H\,I})$ can one obtain a robust estimate of the absorbing gas metallicity as was the case here. While the current observations from both these indicators do not always paint a coherent picture (Péroux et al. 2016), it might also well be that only some of the components in the absorption profile can be explained by one or the other of the scenarios proposed above.

Second, it appears that studies at low redshift provide a good strategy to reach a complete understanding of the relation of the absorbing gas to galaxies. Indeed, at redshift $z < 1$ current

observations can access faint galaxies at the same redshift as the absorber down to $L/L_* \sim 0.01$, allowing a more comprehensive picture of the absorber environment to be assembled than is possible at $z > 1$. For the brightest member in the structure, detailed morphokinematic properties can be derived in a short observing time which would not be possible at higher redshifts. Finally, the MUSE optical coverage means that at $z < 0.8$, the lines of [O II], Hβ and [O III] are covered leading to robust redshift, SFR and metallicity estimates in emission.

6 CONCLUSION

The results presented in this work can be summarized as follows.

(i) We have obtained integral field spectroscopic observations with the VLT/MUSE instrument of a $\sim$1 arcmin field centred on the quasar Q2131−1207. The sightline to this quasar intersects a sub-DLA absorber at $z_{abs} = 0.42980$, characterized by neutral hydrogen column density $\log [N(\text{H I})]/\text{cm}^{-2} = 19.50 \pm 0.15$ and abundance $[\text{X/H}] = -0.54 \pm 0.18$. Approximately 0.1 per cent of the absorbing gas is in molecular form.

(ii) We identify four galaxies at redshifts consistent with that of the sub-DLA absorber, where only one (the brightest of the four) was known previously. The two galaxies closest to the quasar sightline (52 and 61 kpc) exhibit signs of on-going star formation; while the other two, which are further away at projected distances of >140 kpc, are passive galaxies. We report the metallicities of the H II regions of the closest of these objects ($12 + \log(\text{O/H}) = 8.98 \pm 0.02$ and 8.32 ± 0.16) which are to be compared with the metallicity measured in absorption in the neutral phase of the gas ($12 + \log(\text{O/H}) = 8.15 \pm 0.20$). For galaxy 'a', we derive a flat metallicity gradient of $+0.01 \pm 0.03$ dex kpc^{-1}.

(iii) For the brightest object, dubbed galaxy 'a', a detailed morphological analysis indicates that the object is an extended galaxy showing indications of substructure on scales of 1 arcsec. The kinematical modelling shows that it is an inclined ($\sin i = 0.87 \pm 0.01$) large rotating disc with $V_{max} = 200 \pm 3\,\text{km s}^{-1}$. We measure the dynamical mass of the object to be $M_{dyn} = 7.4 \pm 0.4 \times 10^{10}\,\text{M}_\odot$ while the halo mass is $M_{halo} = 2.9 \pm 0.2 \times 10^{12}\,\text{M}_\odot$.

(iv) Some of the gas seen in absorption is likely to be corotating with galaxy 'a', possibly due to a warped disc. In addition, we measure an azimuthal angle of $12° \pm 1°$ which may suggest that some fraction of the absorption may arise in gas being accreted (Péroux et al. 2016). This is further supported by the galaxy to gas metallicity difference, where the metallicity of the gas is found to be lower than the one from the galaxy. We exclude outflows as a possibility to explain the gas in absorption but speculate that some of it may be related to intragroup gas or filament based on indications of a large structure (at least 200 kpc wide) formed by the four galaxies.

(v) Our new observations of the field indicate that the closest object to the quasar line-of-sight (a dwarf galaxy at $z_{gal} = 0.74674$) is unrelated to the absorber. This chance alignment once more calls for caution when associating absorbers with galaxies without spectroscopic information.

Finally, it is clear from the work presented here that further MUSE observations of low-redshift ($z < 0.8$) absorbers in quasar fields hold great potential for constraining the properties of the CGM of galaxies.

REFERENCES

Aguirre A., Hernquist L., Schaye J., Weinberg D., Katz N., Gardner J., 2001, ApJ, 560, 599

Asplund M., Grevesse N., Sauval A., Scott P., 2009, ARA&A, 47, 481

Becker G. D., Bolton J. S., Lidz A., 2015, Publ. Astron. Soc. Aust., 32, e045

Bergeron J., 1986, A&A, 155, 8

Bielby R., Crighton N. H. M., Fumagalli M., Morris S. L., Stott J. P., Tejos N., Cantalupo S., 2016, MNRAS, preprint (arXiv:1607.03386)

Bordoloi R. et al., 2011, ApJ, 743, 10

Bouché N. N., Murphy M., Péroux C., Davies R., Eisenhauer F., Forster-Schreiber N., Tacconi L., 2007, ApJ, 669, L5

Bouché N., Murphy M., Péroux C., Contini T., Martin C., Dessauges-Zavadsky M., 2013, Science, 341, 50

Bouché N., Carfantan H., Schroetter I., Michel-Dansac L., Contini T., 2015, Astrophysics Source Code Library, record ascl:1501.014

Brook C. B. et al., 2011, MNRAS, 415, 1051

Cabanac R. A., Valls-Gabaud D., Lidman C., 2008, MNRAS, 386, 2065

Cowie L. L., Barger A. J., Hu E. M., 2010, ApJ, 711, 928

Deharveng J.-M. et al., 2008, ApJ, 680, 1072

Diamond-Stanic A. M., Coil A. L., Moustakas J., Tremonti C. A., Sell P. H., Mendez A. J., Hickox R. C., Rudnick G. H., 2016, ApJ, 824, 24

D'Odorico V. et al., 2013, MNRAS, 435, 1198

Epinat B. et al., 2009, A&A, 504, 789

Erb D., Shapley A., Pettini M., Steidel C., Reddy N., Adelberger K., 2006, ApJ, 644, 813

Fumagalli M., Cantalupo S., Dekel A., Morris S. L., O'Meara J. M., Prochaska J. X., Theuns T., 2016, MNRAS, 462, 1978

Guillemin P., Bergeron J., 1997, A&A, 328, 499

Heckman T. M., Alexandroff R. M., Borthakur S., Overzier R., Leitherer C., 2015, ApJ, 809, 147

Husemann B., Bennert V. N., Scharwächter J., Woo J.-H., Choudhury O. S., 2016, MNRAS, 455, 1905

Jenkins E. B., 2009, ApJ, 700, 1299

Jenkins E. B., Drake J. F., Morton D. C., Rogerson J. B., Spitzer L., York D. G., 1973, ApJ, 181, L122

Kacprzak G. G., Churchill C. W., Evans J. L., Murphy M. T., Steidel C. C., 2011, MNRAS, 416, 3118

Keating L. C., Haehnelt M. G., Cantalupo S., Puchwein E., 2015, MNRAS, 454, 681

Kennicutt R. C., Jr, 1998, ARA&A, 36, 189

Keres D., Katz N., Weinberg D., Davé R., 2005, MNRAS, 363, 2

Kobulnicky H., Kennicutt R., Pizagno J., 1999, ApJ, 514, 544

Ledoux C., Petitjean P., Srianand R., 2003, MNRAS, 346, 209

Lehner N., Howk J. C., 2011, Science, 334, 955

Lin H., Kirshner R. P., Shectman S. A., Landy S. D., Oemler A., Tucker D. L., Schechter P. L., 1996, ApJ, 464, 60

McGaugh S., 1991, ApJ, 380, 140

Martin C., Shapley A., Coil A., Kornei K., Bundy K., Weiner B., Noeske K., Schiminovich D., 2012, ApJ, 760, 127

Mo H. J., White S. D. M., 2002, MNRAS, 336, 112

Møller P., Fynbo J. U., 2001, A&A, 372, L57

Muzahid S., Kacprzak G. G., Charlton J. C., Churchill C. W., 2016, ApJ, 823, 66

Oppenheimer B., Davé R., 2006, MNRAS, 373, 1265

Pagel B. E. J., Edmunds M. G., Blackwell D. E., Chun M. S., Smith G., 1979, MNRAS, 189, 95

Péroux C., Dessauges-Zavadsky M., Kim T., D'Odorico S., McMahon R., 2003, Mem. Soc. Astron. Ital. Suppl., 3, 261

Péroux C., Dessauges-Zavadsky M., DÓdorico S., Kim T., McMahon R., 2005, MNRAS, 363, 479

Péroux C., Bouché N., Kulkarni V., York D., Vladilo G., 2011a, MNRAS, 410, 2237

Péroux C., Bouché N., Kulkarni V., York D., Vladilo G., 2011b, MNRAS, 410, 2251

Péroux C., Bouché N., Kulkarni V., York D., Vladilo G., 2012, MNRAS, 419, 3060

Péroux C., Bouché N., Kulkarni V., York D., 2013, MNRAS, 436, 2650

Péroux C., Kulkarni V. P., York D. G., 2014, MNRAS, 437, 3144

Péroux C. et al., 2016, MNRAS, 457, 903

Pettini M., 2003, Cosmochemistry: The Melting Pot of Elements. Cambridge Univ. Press, New York

Pettini M., Pagel B., 2004, MNRAS, 348, 59

Pettini M., Shapley A., Steidel C., Cuby J., Dickinson M., Moorwood A., Adelberger K., Giavalisco M., 2001, ApJ, 554, 981

Pettini M., Rix S. A., Steidel C. C., Adelberger K. L., Hunt M. P., Shapley A. E., 2002, ApJ, 569, 742

Quiret S. et al., 2016, MNRAS, 458, 4074

Rahmani H. et al., 2016, MNRAS, 463, 980

Rao S., Turnshek D., Nestor D., 2006, ApJ, 636, 610

Rauch M. et al., 2008, ApJ, 681, 856

Richter P., Fox A. J., Ben Bekhti N., Murphy M. T., Bomans D., Frank S., 2014, Astron. Nachr., 335, 92

Rubin K. H. R., Prochaska J. X., Ménard B., Murray N., Kasen D., Koo D. C., Phillips A. C., 2011, ApJ, 728, 55

Rubin K. H. R., Hennawi J. F., Prochaska J. X., Simcoe R. A., Myers A., Lau M. W., 2015, ApJ, 808, 38

Rupke D. S. N., Kewley L. J., Chien L.-H., 2010, ApJ, 723, 1255

Ryan-Weber E., Pettini M., Madau P., Zych B., 2009, MNRAS, 395, 1476

Sancisi R., Fraternali F., Oosterloo T., van der Hulst T., 2008, A&AR, 15, 189

Schroetter I., Bouché N., Péroux C., Murphy M., Contini T., Finley H., 2015, ApJ, 804, 83

Shapley A. E., Steidel C. C., Pettini M., Adelberger K. L., 2003, ApJ, 588, 65

Shen S., Madau P., Aguirre A., Guedes J., Mayer L., Wadsley J., 2012, ApJ, 760, 50

Shull J. M., 2014, ApJ, 784, 142

Shull J., Danforth C., Tilton E., 2014, ApJ, 796, 49

Simard L. et al., 2002, ApJS, 142, 1

Som D., Kulkarni V., Meiring J., York D., Péroux C., Lauroesch J., Aller M., Khare P., 2015, ApJ, 806, 25

Soto K. T., Lilly S. J., Bacon R., Richard J., Conseil S., 2016, MNRAS, 458, 3210

Spitzer L., Jr, Fitzpatrick E. L., 1995, ApJ, 445, 196

Steidel C., Erb D., Shapley A., Pettini M., Reddy N., Bogosavljevic M., Rudie G., Rakic O., 2010, ApJ, 717, 289

Steidel C., Bogosavljevic M., Shapley A., Kollmeier J., Reddy N., Erb D., Pettini M., 2011, ApJ, 736, 160

Stewart K. R., Kaufmann T., Bullock J. S., Barton E. J., Maller A. H., Diemand J., Wadsley J., 2011, ApJ, 738, 39

Verhamme A., Schaerer D., Atek H., Tapken C., 2008, A&A, 491, 89

Vladilo G., Centurión M., Levshakov S., Péroux C., Kulkarni V., York D., 2006, A&A, 454, 151

Weilbacher P., 2015, in Science Operations 2015: Science Data Management – An ESO/ESA Workshop. ESO, Garching, id. 1, p. 1

Weymann R. J., Williams R. E., Peterson B. M., Turnshek D. A., 1979, ApJ, 234, 33

Wisotzki L. et al., 2016, A&A, 587, A98

Zych B., Murphy M., Pettini M., Hewett P., Ryan-Weber E., Ellison S., 2007, MNRAS, 379, 1409

## APPENDIX A: MUSE GALAXY SPECTRA UNRELATED TO THE QUASAR ABSORBER

This appendix presents two MUSE spectra of objects unrelated to the quasar absorber at $z_{abs} = 0.42980$. The first is a dwarf galaxy that is nearer to the quasar slightline than any of the four galaxies discussed in the main text (at impact parameter $\delta = 2.06$ arcsec). The object shows a number of strong emission lines including [O II], [Ne III] $\lambda3871$, Hδ, Hβ, [O III] at $z_{gal} = 0.74674$, i.e. higher than the redshift of the quasar. A portion of our MUSE spectrum of that object is reproduced in Fig. A1.

Given the MUSE wavelength coverage, the most prominent absorption lines associated with the sub-DLA which are covered are the Ca II H&K lines. We recall that Muzahid et al. (2016) report log N(Ca II) $= 11.98 \pm 0.10$ based on the Keck/HIRES spectra. The doublet is also clearly visible in the MUSE spectrum of the background quasar. However, notwithstanding the high S/N of the nearby dwarf galaxy spectrum at these wavelengths, we do not detect the Ca II doublet in absorption along this adjacent sightline, separated by 11.6 kpc from the quasar sightline at the redshift of the sub-DLA. We calculate that given the quality of the spectrum we should only be able to measure N(Ca II) > 12.09 at 3σ, so that the non-detection is consistent with the higher resolution measurement in the quasar spectrum. We note that in the future such bright objects will be of use to probe the gas in absorption against multiple background sources.
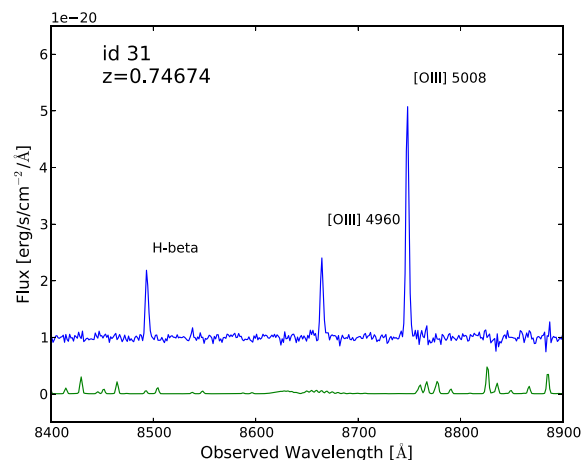
Figure A1. MUSE spectrum of a dwarf galaxy. The object lies at an impact parameter $\delta = 2.06$ arcsec away from the quasar line-of-sight and is clearly detected in the *HST*/WFPC2 images (see Fig. 3). The numerous emission lines are used to constrain the redshift to be $z_{gal} = 0.74674$, i.e. higher than the redshift of the quasar.
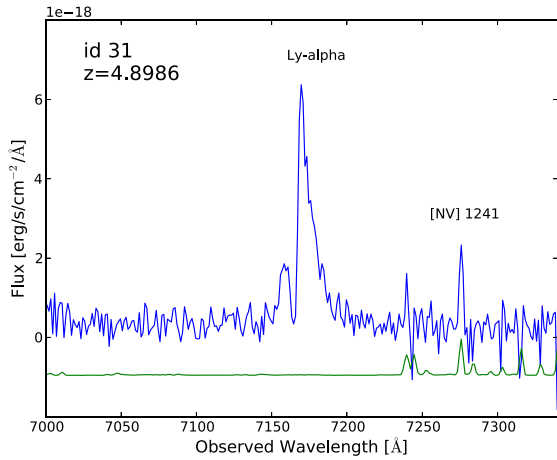
Figure A2. MUSE spectrum of a strong emitter, coincident with the red-shifted wavelength of [O III] λ5008 at the redshift of the sub-DLA. The emission line shown is undoubtedly Lyα from a galaxy at $z_{gal} = 4.8986$, as indicated by the characteristic asymmetric emission+absorption line profile and the presence of narrow N V λ1240.81 emission. This object is marked as 'LAE' in Fig. 5 and shown with a red arrow in Fig. 6.

The second object appears to be coincident with the redshifted wavelength of [O III] λ5008 at the redshift of the sub-DLA. However, the emission line is undoubtedly Lyα from a galaxy at $z_{gal} = 4.8986$, as indicated by the characteristic asymmetric emission+absorption line profile (Verhamme et al. 2008) and the presence of narrow N V λ1240.81 emission (Fig. A2).

This paper has been typeset from a TEX/LATEX file prepared by the author.